Microstructural and Mechanical Properties of a Beta-type Titanium Alloy Joint Fabricated by Friction Stir Welding

Huihong Liu, Hidetoshi Fujii

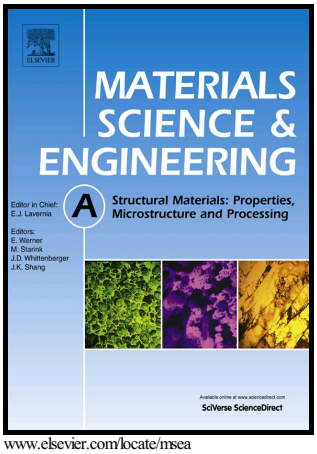

www.elsevier.com/locate/msea

PII: S0921-5093(17)31455-7
DOI: https://doi.org/10.1016/j.msea.2017.11.006
Reference: MSA35721

To appear in: *Materials Science & Engineering A*

Received date: 27 August 2017
Revised date: 1 November 2017
Accepted date: 3 November 2017

Cite this article as: Huihong Liu and Hidetoshi Fujii, Microstructural and Mechanical Properties of a Beta-type Titanium Alloy Joint Fabricated by Friction Stir Welding, *Materials Science & Engineering A*, https://doi.org/10.1016/j.msea.2017.11.006

Microstructural and Mechanical Properties of a Beta-type Titanium Alloy Joint Fabricated by Friction Stir Welding

Huihong Liu, Hidetoshi Fujii

Joining and Welding Research Institute, Osaka University, Ibaraki, Osaka, 567-0047, Japan

Abstract

Friction stir welding (FSW) was performed on β-type Ti-15V-3Cr-3Al-3Sn alloy (Ti-15-3, mass%) plates to fabricate a sound weld joint. The microstructural and mechanical properties of the weld joint were systematically investigated in order to understand the response of the β-type titanium alloys to the FSW. The results show that a defect-free Ti-15-3 alloy weld joint can be successfully fabricated by the FSW. In the thermo-mechanically affected zone (TMAZ), the microstructural evolution is predominantly driven by discontinuous dynamic recrystallization because of the low stacking fault energy of the alloy that results in a low dislocation mobility; while in the stir zone (SZ) it is mainly promoted by continuous dynamic recrystallization due to the high temperature and high strain achieved in the SZ which improve the dislocation mobility. The material flow field within the SZ shows an incline of ~10° towards the advancing side (AS) around the welding direction (WD). The base material and the weld-associated zones (TMAZ and SZ) show comparable mechanical properties, which is due to the competitive effects of the dislocation density, grain diameter and grain orientation. This homogeneous mechanical property distribution makes the Ti-15-3 alloy joint preferred for industrial applications.

Keywords: Beta-type titanium alloys, friction stir welding, microstructure, mechanical properties

1. Introduction

Titanium and its alloys have been widely commercially used in a broad range of aerospace applications and biological applications because of their good mechanical properties, great specific strength, high corrosion resistance, as well as the most excellent biocompatibility among metallic biomaterials [1-6]. Among them, since Ti-15V-3Cr-3Al-3Sn (Ti-15-3, mass%), as a commercial metastable β (body center cubic: bcc)-type titanium alloy, possesses an excellent cold formability, which contributes to reducing the manufacturing and fabrication costs and a great aging strengthening response that enables it to obtain a high strength by proper aging treatment, it is receiving increasing attention for use in aircraft applications as an alternative to the conventionally used titanium alloys [7-10]. Welding is therefore necessary for the titanium's industrial applications.

Titanium and its alloys are generally considered as weldable by conventional fusion welding [11]. However, it has been reported [11-14] that the fusion welding can cause several issues such as the formation of a coarse microstructure with columnar grains, high residual stress, severe welding distortion due to the low thermal conductivity, solidification defects, titanium oxide due to the high reactivity, as well as solute segregation occurring during solidification, in particular, in the β-stabilizer-rich titanium alloys such as Ti-15-3, which inevitably deteriorate the quality of the weld joints of titanium and its alloys. Friction stir welding (FSW) [15], which was invented by The Welding Institute (TWI) in 1991, is an innovative joining technique enabling solid-state joining, thereby it avoids or minimizes the fusion-welding-associated problems. To date, the

FSW has been extensively studied on the low-melting-point materials such as aluminum, magnesium and their alloys [16-20]. However, for high-melting-point materials such as iron, titanium and their alloys, the FSW study is still limited especially for the latter because more durable tools at high temperature are strongly required. In recent years, with the tool development, iron, titanium and their alloys have been successfully FSWed using high temperature durable tools such as coated TiC tools and WC-based alloy tools. For example, Lee et al. [21] succeeded in fabricating pure titanium joints using FSW. Fujii et al. [11] investigated the microstructure and mechanical properties of the FSWed pure titanium joints fabricated at various welding conditions. Mironov et al. [22] examined the microstructural evolution in the β-phase field during the FSW of the Ti-6Al-4V alloy and reported that the grain structural development in the β-phase field is presumably driven by grain elongation and transverse grain subdivision. However, these FSW studies of titanium and its alloys have mainly focused on the pure α (hexagonal close packed: hcp)-type titanium and the (α+β)-type Ti-6Al-4V alloy. The FSW of the β-type titanium alloys is apparently necessary to be systematically studied for our comprehensive understanding of the FSW of titanium and its alloys.

In the present study, FSW processing was performed on the β-type Ti-15-3 alloy plates in order to fabricate a sound weld joint. The microstructural and mechanical properties of the weld joint were systematically investigated to clarify the response of the β-type titanium alloys to the FSW.

2. Experimental procedures

As received annealed Ti-15-3 alloy plates, 150 mm long, 50 mm wide and 1.45 mm thick, were used as the base material (BM) in this study. The chemical composition of the alloy is shown in Table 1. The alloy plates were butt-friction-stir-welded as illustrated in Fig. 1a at a rotation speed

of 250 rpm and a welding speed of 50 mm/min under load control. The FSW geometry described by the welding direction (WD), transverse direction (TD) and normal direction (ND) is also shown in Fig. 1a. The tool rotation axis was tilted by 3° towards the tool traverse direction. An argon shielding gas was flowed around the tool during the welding in order to prevent the joint surface from being oxidized. The welding tool applied in this study was made of a WC-based alloy and had a 12 mm should diameter, a 4 mm probe diameter, and a 1.3 mm probe length.

The cross-section specimen of the weld joint perpendicular to the WD was prepared using an electrical discharge machine (EDM), then subjected to the microstructural analysis by optical microscopy (OM) and electron backscatter diffraction (EBSD) from the observation direction as indicated in Fig. 1a. The specimen was mechanically polished using waterproof SiC emery papers of up to 4000 grit and mirror polished using a colloidal SiO_2 suspension. The mirror-polished specimen was then etched using an aqueous solution consisting of 1 vol.% HF and 0.5 vol.% HNO_3 for ~1 min and subjected to the OM observation (Olympus BX51). For the EBSD observation (JEOL JSM-7001FA), the specimen was mechanically polished in a similar manner and then electro-polished in a solution consisting of 10 vol.% perchloric acid and 90 vol.% acetic acid at 30 V for ~30 s at room temperature. EBSD maps containing ~320,000–~520,000 pixels and having average confidential indexes (CIs) of 0.54–0.80 were obtained at the scanning step sizes ranging from 0.2 μm to 0.8 μm. In the maps, boundaries with misorientation angles lower than 2° were removed in order to eliminate spurious boundaries caused by orientation noise. In this study, boundaries having misorientation angles equal to or higher than 15° were defined as high-angle grain boundaries (HABs), while those having misorientation angles between 2° and 15° were denoted as low-angle grain boundaries (LABs).

The mechanical properties of the weld joint were evaluated by Vickers hardness test and tensile test. The cross-section specimen was mechanically polished using waterproof SiC emery papers of up to 2400 grit, then the Vickers hardness distribution was examined along the transverse centerline of the cross section under a load of 0.98 N for a dwell time of 15 s. Local tensile specimens with a gauge thickness of ~1.4 mm, a gauge width of 2 mm and a gauge length of 4 mm were cut in both the BM region and the stir zone (SZ) region by an EDM as illustrated in Fig. 1b and mechanically polished in a similar manner as already-mentioned, then they were subjected to the tensile tests at a cross-head speed of 0.2 mm/min in order to evaluate the tensile properties of these two specific regions. A joint tensile specimen of ~1.4 mm gauge thick, 6 mm gauge wide and 25 mm gauge long was also prepared using an EDM as illustrated in Fig. 1b, then tested at a cross-head speed of 1 mm/min to evaluate the tensile properties of the weld joint. Three specimens were used for tensile tests in order to minimize the experimental error.

3. Results and discussion

3.1. Microstructure

The surface appearance and the optical macrograph of the transverse cross section of the weld joint are shown in Fig. 2. No obvious defect can be identified on both the surface and the cross section indicating that a defect-free Ti-15-3 alloy weld joint was successfully fabricated by the FSW. A basin-shaped SZ was observed on the cross section. The SZ borders adjacent to the advancing side (AS) and the retreating side (RS) show slightly different curvatures, which might suggest the occurrence of different material flows within both sides.

Figure 3 shows the EBSD inverse pole figure (IPF) and the corresponding (101) and (111) pole figures (PFs) of the BM. The black and white lines shown in the IPF represent the HABs and

LABs, respectively, and in all subsequent figures. A microstructure consisting of both equiaxed grains and elongated grains as well as a number of LABs accounting for 55% of the total grain boundary length is identified in the BM. The PFs indicate that the BM possesses a rolling texture containing both the <101>//rolling direction (RD) which is parallel to the WD and <111>//ND components.

The microstructure of the thermo-mechanically affected zone (TMAZ) adjacent to the RS obtained by EBSD observations is shown in Fig. 4. Three distinct regions showing different microstructural characteristics are identified as indicated by the dotted curved lines. Region 1, which is considered to belong to the BM, shows a microstructure composed of relatively low-aspect-ratio grains having an average grain diameter of ~30 μm with a low LAB density, while region 3, the edge of the SZ, possesses mostly small equiaxed grains (~5 μm) accompanied with a relatively high LAB density. In region 2, both large elongated grains having a long axis of tens of microns and relatively small equiaxed grains with grain diameters of several microns surrounding the elongated grains are observed; hence, region 2 is regarded as the TMAZ. A high LAB density can also be confirmed in this region which contains abundant and dense substructures. Three local areas within the TMAZ marked by the dotted rectangles are magnified in Figs. 4b, 4c, and 4d. Not only based on Fig. 4b, but also many other areas of the TMAZ, it is seen that most of the LABs show irregular shapes rather than well-arranged shapes. Moreover, in most grains, the LABs tend to aggregate near the elongated boundaries, then boundary bulging occurs via boundary migration. Four boundary bulging positions in one parent grain are indicated by the arrows marked in Fig. 4b, and the misorientation angles as a function of the distances along the arrows are measured in Fig. 4e. These results show that the HABs gradually form and tend to complete between the bulged region and the parent grain, and the misorientation angles

between them gradually increase in the order of (1), (2), (3) and (4). This phenomenon clearly demonstrates a recrystallized grain formation process via grain boundary bulging, in which the boundary migration is driven by the large difference in the stored strain energy on different sides of the boundary, then massive dislocations are absorbed into the bulging boundary making the bulged region rotate, which increases the misorientation between the bulged region and the parent region and finally produces a new grain with the HABs. On the other hand, the LAB to HAB transformation that occurs via subgrain rotation can also be observed only within a few grains as shown in Figs. 4c and 4d. It is noted that the grain indicated by the arrow in Fig. 4c might form either by a subgrain-rotation-induced LAB to HAB transformation or by direct HAB grain nucleation through energy fluctuation. Based on the above-mentioned results, therefore, it is concluded that the microstructural evolution in the TMAZ is predominantly driven by the discontinuous dynamic recrystallization (DDRX).

Figure 5 shows the microstructure of the SZ of the weld joint obtained by EBSD observations. Several locations throughout the SZ including top (a), center (b) and bottom (c) of the SZ-center, and RS (d) and AS (e) of the SZ as illustrated in Fig. 5a were examined. It can be seen that both equiaxed and fibrous-shaped recrystallized grains are observed throughout the SZ. Most LABs show well-arranged structures rather than irregular structures. In many fibrous-shaped grains, the LAB arrays lying transversely along the short axis and/or LAB to HAB segment transformation can be identified as shown in the inset magnified images, which suggests that the grain subdivision [23, 24] occurs throughout the SZ. Therefore, the microstructural evolution in the SZ is considered to be mainly driven by the continuous dynamic recrystallization (CDRX).

The corresponding (101) PFs of all the examined locations within the SZ are exhibited in the left half of the rectangular frames in Fig. 6 in order to evaluate the texture distribution throughout the

SZ. These PFs have a reference frame in which the ND is vertical and the TD is horizontal, the same as that in the OM and EBSD micrographs. It is known that the predominant deformation mode within the SZ during FSW is generally regarded as simple shear even though the material flow during the FSW seems complicated [25-27]. Shear texture is conventionally defined in terms of the crystallographic plane {hkl} and direction <uvw> parallel to the shear plane and shear direction (SD), respectively; the corresponding PF has a reference frame in which the shear plane normal (SPN) is shown vertical and the SD is horizontal. During the FSW, the shear plane within the SZ has been reported [28, 29] to align with the surface of a truncated cone (as indicated by the yellow dotted lines shown in Fig. 6a) which has a diameter close to the tool shoulder diameter in the top of the SZ and a diameter similar to that of the probe in the bottom of the SZ. It can be seen that the angle between the SPN and ND is ~15° on the RS/TMAZ border, while it is ~14° on the AS/TMAZ border. The SD is regarded to align with a circle of the horizontal section of the truncated cone [28, 29]; hence, the SD is known to be parallel to the WD in the extremity of the RS and AS, and aligns with the TD in the SZ-center. Based on these abovementioned views, the original (101) PFs obtained in the top (Fig. 6b), center (Fig. 6c) and bottom (Fig. 6d) of the SZ-center along the plate thickness direction were rotated by 15° around the TD to align the SPN vertical in order to correspond to the conventional reference frame of simple shear. The rotated PFs (not shown here) show the characteristic poles close to but still slightly deviated from the projections of the D_2 $(11\bar{2})[111]$ ideal simple shear texture component of the bcc metals as illustrated in Fig. 6g [30, 31]. These rotated PFs were finally adjusted by suitable rotations to well match the ideal projections, as shown in the right half of the rectangular frames in Fig. 6; the rotation angles are specifically summarized. It is noted that, along the plate thickness direction, the rotation angle around the TD slightly gradually decreases from the top to

bottom, while that around the WD maintains a constant value of 10°. For the PFs of the RS and AS, since the EBSD maps were not taken in the extremity, the SD was not directed towards the WD, but somehow deviated from it. As illustrated in 90°-tilted half-circle SD curvature shown in Fig. 6a, the angle between SD and TD is around 46° (clockwise) in the RS, and approximately -40° (counterclockwise) in the AS. Therefore, the original (101) PFs of the RS and AS were rotated by 15° and 14° around the TD, then by 46° and -40° around the ND, respectively, to make the SPN vertical and the SD horizontal. Similar to those PFs of the SZ-center, these rotated PFs (not shown) were also slightly adjusted into very close correspondence. It is seen that the rotation angle around the TD decreases from the RS to AS gradually along the transverse direction. The final corrected (101) PFs suggest that all the locations examined throughout the SZ show a similar pattern which can be described as a superposition of the {110}<uvw> and {hkl}<111> fiber components of ideal simple shear textures, and the D_2 $(11\bar{2})[111]$ component is predominant among them.

3.2. Mechanical properties

The hardness distribution was examined along the transverse center line on the cross section of the joint and the result is shown in Fig. 7a. It is found that the hardness almost remains constant at approximately 260 Hv and no obvious softened region is identified along the transverse center line. The tensile properties of the BM local specimens and SZ local specimens are shown in Fig. 7b. The SZ local specimens show tensile strength (σ_b) of ~860 MPa, yield strength (σ_y) of ~850 MPa, and elongation (ε) of ~20%, which are comparable to those of the BM local specimens that exhibit tensile strength of ~850 MPa, yield strength of ~845 MPa, and elongation of ~25%. Although the tensile properties were not determined for the TMAZ since it is quite difficult, the

hardness of the TMAZ is shown to be comparable to those of the BM and the SZ. It is known that in the absence of appreciable work hardening, the hardness of a material, Hv, as measured using a pyramidal indenter is proportional to the yield strength through the expression [32, 33] of $Hv \approx 3\sigma_y$, to which the hardness (~260 Hv) and the yield strength (~850 MPa) of the BM and the SZ shown in the present study well match, thus the TMAZ is reasonably considered to have tensile properties comparable to the BM and the SZ. These results indicate that a sound Ti-15-3 joint, which has a quite homogenous distribution of mechanical properties along the transverse direction across the BM and the weld-associated zones including TMAZ and SZ, was successfully produced by the FSW. The joint tensile specimen was also tested and the tensile fracture was observed to take place in the BM region as shown in the fractured specimen image (Fig. 7c), which is attributed to the slightly higher hardness and higher tensile strength obtained in the SZ compared to those of the BM.

3.3. Discussion

3.3.1. Microstructural evolution in the TMAZ and SZ

It has already been mentioned that the microstructural development in the TMAZ is mainly driven by the DDRX since the occurrence of recrystallization via boundary bulging and substructures consisting of irregular-shaped LABs are extensively confirmed in this region. This is because the Ti-15-3 alloy, as a β-type titanium alloy, possesses a low stacking fault energy [34], that facilitates the dissociation of full dislocations into partial ones and makes the cross-slip and climb of dislocations difficult. Therefore, the CDRX, which generally occurs via well-arranged LAB substructure formation and rotation requiring the dislocation annihilation and arrangement, is not preferred in this alloy due to its low dislocation mobility. However, within

the SZ, the microstructural evolution mainly occurs via the CDRX. This is likely to be due to the fact that a higher deformation strain and a higher temperature were introduced into the SZ, thus enhancing the dislocation mobility and facilitating the occurrence of the CDRX.

3.3.2. Texture distribution within the SZ

The final corrected (101) PFs indicate that the entire SZ shows a similar shear texture composed of {110}<uvw> and {hkl}<111> fiber components, and the D_2 $(11\bar{2})[111]$ component is the predominant one among them. This suggests that the {112}<111> dislocation slip mainly occurs within the SZ during the FSW, thus inducing the formation of the $(11\bar{2})[111]$ simple shear texture component predominantly. Different maximum texture intensities are obtained for each examined location within the SZ as shown in Fig. 6. It is known that the texture formation and evolution within the SZ during the FSW should be closely correlated with the material flow behaviors [35-38], hence the relationship between the texture intensity and the material flow within the SZ is discussed. The material flow patterns on the horizontal top-plane, mid-plane and bottom-plane of the SZ have been investigated both experimentally and theoretically [39, 40], as illustrated in Figs. 8a, 8b and 8c, respectively. For the top-plane, a round flow zone (indicated by grey rings around the probe) generates around the probe and the material flow bypasses around the round flow zone, while on the bottom-plane, no round flow zone forms and the material flow bypasses around the probe. The mid-plane shows a transient material flow pattern between those on the top- and bottom-planes. It has been reported [40] that the temperature and the strain of the material increase as the material flow distance increases. The material on the AS marked by circle 1 in Fig. 8b is thus known to have a higher temperature and a higher strain compared to that in the RS indicated by circle 2 because the material flow distance is much longer on the AS.

Therefore, the fact that the shear texture on the AS shows a higher intensity than that on the RS suggests that the higher strain achieved on the AS plays a predominant role in introducing a higher texture intensity. It is noted that the center of the SZ-center marked by circle 3 has a texture intensity comparable with that on the AS. Since the center of the SZ-center possesses a moderate strain and temperature between the RS and the AS, it is concluded that, in addition to the strain, the temperature also affects the texture intensity; the high temperature tends to promote the recrystallization thereby weakening the deformation texture in the AS and vise versa in the center of the SZ-center. Similar results can be obtained by analyzing the texture intensity distribution along the plate thickness direction. The top of the SZ-center marked by circle 4 in Fig. 8a has a higher temperature and strain than the bottom of the SZ-center indicated by circle 5 in Fig. 8c. The higher strain in the top mainly contributes to the higher texture intensity compared to that in the bottom. The center of the SZ-center (circle 3), which shows a moderate strain and temperature between the top and the bottom, exhibits a higher texture intensity than the top, which suggests that the relatively lower temperature in the center hinders the recrystallization, thus maintaining a stronger shear texture compared to that in the top.

3.3.3. Material flow field within the SZ

The original (101) PFs taken from several locations within the SZ were suitably rotated to correspond to the conventional reference frame for an ideal simple shear texture based on the views about the truncated-cone-surface shear plane and horizontal-section-circle SD reported in the literatures [28, 29]. The additional suitably-rotated small angles for close matching is likely to be attributed to the rough estimation of the shear plane and SD for a specific location and/or the complicated material flow during the FSW. Since the final rotated PFs match with the conventional reference frame where the SPN is vertical and the SD is horizontal, this reference

frame was reversely rotated by those above-obtained rotation angles, respectively, to recover the actual shear plane and SD for each location in order to reveal the material flow field within the SZ. This newly proposed phrase, "material flow field", does not mean the actual material flow path but the real-time spatial material flow direction for a specific location. The result is shown in Fig. 9, where the SPN and SD are indicated by the blue arrows and red arrows, respectively, the material flow field is illustrated by the black dotted ellipses, and the green dotted straight lines represent the ND and TD in the specimen geometry. It suggests that the material flow field within the SZ shows an incline of approximately 10° towards the AS around the WD. It is noted that, along the transverse direction, the rotation angles around the TD decrease in the order of the RS, center and AS, which can be reasonably explained as the material flow field incline apparently makes the angle between the ND and SPN higher on the RS and lower on the AS. In addition, the rotation angle around the ND in the RS shows a much higher value than that in the AS which is attributed to that the AS observation location gets closer to the SD//TD position compared to the RS observation position because of the material flow field tilting. A similar tilt of material flow has been three-dimensional in-situ visualized in the FSW of pure aluminum by an X-ray transmission real-time imaging system using a tiny spherical tracer [41]. Therefore, the proposed incline of the material flow field is strongly supported and thus quite reasonable.

3.3.4. Relationship between microstructure and mechanical properties of the joint

It is concluded that a very homogeneous mechanical property distribution was achieved along the transverse direction crossing the BM and the weld-associated zones including the TMAZ and SZ in the Ti-15-3 FSW joint. The microstructure of each zone has been shown to be affected by the FSW and is well known to determine the mechanical properties. Thus, the relationship between the microstructure and mechanical properties in the joint was systematically

investigated. Figure 10 shows the microstructural features including the average grain boundary spacing in the TD (a), length fractions of the LAB (b), misorientation angle distributions of the boundaries (c), and average Taylor factors (d) of the different zones including the BM, TMAZ, and all examined locations within the SZ of the joint. The average grain boundary spacing in the TD for the LAB and HAB was measured based on the linear intercept method. It decreases from the BM to TMAZ and to SZ, then almost remains constant within the SZ for both the LAB and HAB. The average grain boundary spacing in the TD for the HAB is reasonably larger than that for the LAB in all the examined regions, and the difference in the value is the highest in the TMAZ, which well matches the coexistence of the large elongated grains, a few small recrystallized grains and the abundant substructures constituting the LABs. Thus, it is inferred that the fine grain strengthening effect, which is inversely proportional to the grain boundary spacing, increases in the order of the BM, TMAZ, and SZ based on the firmly established Hall-Petch equation [42, 43]:

$$\sigma_y = \sigma_0 + k_y d^{-1/2} \quad (1)$$

where σ_y is the yield stress, σ_0 is the friction stress that includes contributions from the solutes and particles, but not from dislocations, k_y is a constant, and d is the grain size. The result of the grain boundary fraction indicates that the length fraction of the LAB first increases from BM (~55%) to TMAZ (~72%), then decreases to a nearly constant value (~32%) in the SZ. The misorientation angle distribution of the boundaries shows a similar result to that obtained from the grain boundary fraction, and the entire SZ exhibits a close misorientation angle distribution of the boundaries. It has been reported [44-46] that the dislocation density in the interior of the grains is determined by the misorientation angle across the dislocation boundaries and the

dislocation boundary area per unit volume. From a more quantitative standpoint, the dislocation density can be approximately characterized by the value calculated according to the equation $\frac{1}{S}\sum\theta \cdot l_b$, where $\sum\theta$ represents the accumulation of the product of the misorientation angle across the dislocation boundaries, i.e. the LABs with misorientation angle ranging from 2° to 15°, and the l_b and S denotes the step size and the area of the EBSD measurements, respectively. It can be seen that the integrated area ranging from 2° to 15° under the misorientation angle distribution profile decreases from the TMAZ to BM then to the SZ, thus the dislocation density of each zone is regarded to show the same variation tendency, i.e. decreasing in the order of the TMAZ, BM, and SZ. The strength increment, $\Delta\sigma_y$, in a material due to the increased dislocation density, ρ, can be described as follows [47-49]:

$$\Delta\sigma_y = M\alpha Gb\rho^{1/2} \quad (2)$$

in which M is the Taylor factor, α is a constant, G is the shear modulus and b is the Burgers vector. Thus, the dislocation strengthening effect, which is proportional to the dislocation density, also shows a decreased tendency in the order of the TMAZ, BM, and SZ. Furthermore, the average Taylor factor is found to decrease from the BM to TMAZ, then recovers to a relatively high value throughout the SZ; i.e. the TMAZ exhibits the lowest Taylor factor among all the examined regions. The Taylor factor is known as an orientation factor which is normally used to relate the yield strength, σ_y, of polycrystals of cubic metals to the critical resolved shear stress (CRSS), τ_0, of a reference single crystal, described as $M = \frac{\sigma_y}{\tau_0}$ [50, 51]. It is related to the texture and the orientation of the tensile axis relative to the specimen axis, that denotes the effect of texture on the mechanical properties [52, 53]. Thus, in combination with equation (2), the orientation strengthening effect, that is proportional to the Taylor factor value, decreases from

the BM to TMAZ, then increases into the SZ. Based on these results, it is therefore concluded that the comparable mechanical properties obtained in the BM, TMAZ, and SZ are attributed to the competitive effects from the dislocation density, grain size, and grain orientation. It is known [54] that a mechanical property gap between the BM and TMAZ or the TMAZ and SZ facilitates the occurrence of a stress concentration in the zone border during loading because the coordinate deformation between the zones is limited, which deteriorates the fatigue properties and also the elongation of the FSW joint. Nakai et al. [54] adopted a post-weld heat treatment on a Ti-6Al-4V FSW joint to homogenize the microstructure and mechanical properties of the BM and SZ and successfully modified the fatigue properties of the joint. Thus, in the present study, the resulting homogenous mechanical property distribution along the transverse direction across the BM and the weld-associated zones will make the Ti-15-3 FSW joint sound and preferred for industrial applications.

4. Conclusions

In the present study, the β-type Ti-15-3 alloy plates were subjected to FSW processing in order to obtain a sound weld joint. The microstructural and mechanical properties of the weld joint were systematically characterized to understand the response of the β-type titanium alloys to the FSW. The obtained conclusions are as follows:

[1] A defect-free, sound weld joint of β-type Ti-15-3 alloy was successfully fabricated by FSW.

[2] In the TMAZ, the microstructural evolution during the FSW is predominantly driven by discontinuous dynamic recrystallization because of the low stacking fault energy of the alloy and the resulting low dislocation mobility; while in the SZ, the microstructural development was mainly promoted by continuous dynamic recrystallization, which is due to the high temperature

and high strain achieved in the SZ enhancing the dislocation mobility thereby facilitating the occurrence of continuous dynamic recrystallization.

[3] The SZ shows a shear texture consisting of the superposition of {110}<uvw> and {hkl}<111> fiber components of ideal simple shear textures and the D_2 $(11\bar{2})[111]$ component is the predominant one among them.

[4] The material flow field within the SZ shows an incline of approximately 10° towards the AS around the WD.

[5] The BM and the weld-associated regions including the TMAZ and SZ show comparable mechanical properties, which is attributed to the competitive effects of the dislocation density, grain diameter and grain orientation, that makes the Ti-15-3 alloy joint preferred for industrial applications.

Acknowledgement

The authors wish to acknowledge the financial support by the Japan Science and Technology Agency (JST), the Global COE Programs from the Ministry of Education, Sports, Culture, Science, and a Grant-in-Aid for Science Research from the Japan Society for Promotion of Science and Technology of Japan, ISIJ Research Promotion Grant.

References:

[1] R.R. Boyer, An overview on the use of titanium in the aerospace industry, Mater. Sci. Eng. A 213 (1996) 103-114.

[2] J.C. Williams, E.A. Starke, Progress in structural materials for aerospace systems, Acta Mater. 51 (2003) 5775-5799.

[3] M. Niinomi, M. Nakai, J. Hieda, Development of new metallic alloys for biomedical applications, Acta Biomater. 8 (2012) 3888-3903.

[4] M. Niinomi, Recent research and development in titanium alloys for biomedical applications and healthcare goods, Sci. Technol. Adv. Mater. 4 (2003) 445-454.

[5] H.H. Liu, M. Niinomi, M. Nakai, K. Cho, K. Narita, M. Sen, H. Shiku, T. Matsue, Mechanical properties and cytocompatibility of oxygen-modified β-type Ti-Cr alloys for spinal fixation devices, Acta Biomater. 12 (2015) 352-361.

[6] H.H. Liu, M. Niinomi, M. Nakai, X. Cong, K. Cho, C.J. Boehlert, V. Khademi, Abnormal deformation behavior of oxygen-modified β-type Ti-29Nb-13Ta-4.6Zr alloys for biomedical applications, Metall. Mater. Trans. A 48 (2017) 139-149.

[7] J.D. Cotton, R.D. Briggs, R.R. Boyer, S. Tamirisakandala, P. Russo, N. Shchetnikov, J.C. Fanning, State of the art in beta titanium alloys for airframe applications, JOM 67 (2015) 1281-1303.

[8] H.W. Rosenberg, Ti-15-3: A new cold-formable sheet titanium alloy, JOM 35 (1983) 30-34.

[9] R.R. Boyer, Aerospace applications of beta titanium alloys, JOM 46 (1994) 20-23.

[10] S.M. Kazanjian, E.A. Starke, Effects of microstructural modification on fatigue crack growth resistance of Ti-15V-3Al-3Sn-3Cr, Int. J. Fatigue 21 (1999) S127-S135.

[11] W.A. Baeslack III, D.W. Becker, F.H. Froes, Advances in titanium alloy welding metallurgy, JOM 36 (1984) 46-58.

[12] W.A. Baeslack III, J.M. Gerken, C. Cross, J. Hanson, P.S. Liu, J.C. Monses, J. Schley, L. Showalter, Titanium and titanium alloys, in: J.M. Gerken (Ed.), Welding Handbook, vol. 4, eighth edn, American Welding Society, Miami, Florida, USA, 1988, pp. 488-540.

[13] D. Banerjee, J.C. Williams, Perspectives on titanium science and technology, Acta Mater. 61 (2013) 844-879.

[14] R.R. Boyer, R.D. Briggs, The use of β titanium alloys in the aerospace industry, J. Mater. Eng. Perform. 14 (2005) 681-685.

[15] W.M. Thomas, D.E. Nicholas, J.C. Needham, M.G. Murch, P. Templesmith, C.J. Dawes, GB Patent Application No. 9125978.8, Dec. 1991.

[16] Y.S. Sato, H. Kokawa, M. Enomoto, S. Jogan, Microstructural evolution of 6063 aluminum during friction-stir welding, Metall. Mater. Trans. A 30 (1999) 2429-2437.

[17] Y. Li, L.E. Murr, J.C. McClure, Flow visualization and residual microstructures associated with the friction-stir welding of 2024 aluminum to 6061 aluminum, Mater. Sci. Eng. A 271 (1999) 213-223.

[18] H.J.Liu, H.Fujii, M.Maeda and K.Nogi, "Tensile Properties and Fracture Locations of Friction Stir Welded Joints of 2017-T351 Aluminum Alloy", J. Mater. Proc. Tech., 142 (2003) 692-696.

[19] S.H.C. Park, Y.S. Sato, H. Kokawa, Effect of micro-texture on fracture location in friction stir weld of Mg alloy AZ61 during tensile test, Scr. Mater. 49 (2003) 161-166.

[20] D.T. Zhang, M. Suzuki, K. Maruyama, Microstructural evolution of a heat-resistant magnesium alloy due to friction stir welding, Scr. Mater. 52 (2005) 899-903.

[21] W.B. Lee, C.Y. Lee, W.S. Chang, Y.M. Yeon, S.B. Jung, Microstructural investigation of friction stir welded pure titanium, Mater. Lett. 59 (2005) 3315-3318.

[22] S. Mironov, Y. Zhang, Y.S. Sato, H. Kokawa, Development of grain structure in β-phase field during friction stir welding of Ti-6Al-4V alloy, Scr. Mater. 59 (2008) 27-30.

[23] P.J. Hurley, F.J. Humphreys, The application of EBSD to the study of substructural development in a cold rolled single-phase aluminum alloy, Acta Mater. 51 (2003) 1087-1102.

[24] D.A. Hughes, N. Hansen, High angle boundaries formed by grain subdivision mechanisms, Acta Mater. 45 (1997) 3871-3886.

[25] R.W. Fonda, J.F. Bingert, K.J. Colligan, Development of grain structure during friction stir welding, Scr. Mater. 51 (2004) 243-248.

[26] P.B. Prangnell, C.P. Heason, Grain structure formation during friction stir welding observed by the 'stop action technique', Acta Mater. 53 (2005) 3179-3192.

[27] S. Mironov, Y.S. Sato, H. Kokawa, Microstructural evolution during friction stir-processing of pure iron, Acta Mater. 56 (2008) 2602-2614.

[28] A.P. Reynolds, E. Hood, W. Tang, Texture in friction stir welds of Timetal 21S, Scr. Mater. 52 (2005) 491-494.

[29] S. Mironov, Y.S. Sato, H. Kokawa, Development of grain structure during friction stir welding of pure titanium, Acta Mater. 57 (2009) 4519-4528.

[30] S. Li, I.J. Beyerlein, M.A.M. Bourke, Texture formation during equal channel angular extrusion of fcc and bcc materials: comparison with simple shear, Mater. Sci. Eng. A 394 (2005) 66-77.

[31] R.W. Fonda, K.E. Knipling, Texture development in friction stir welds, Sci. Tech. Weld. Join. 16 (2011) 288-294.

[32] M.F. Ashby, D.R.H. Jones, Engineering Materials 1 An Introduction to their Properties and Applications, second ed., Butterworth-Heinemann, Oxford, 1996.

[33] M. Furukawa, Z. Horita, M. Nemoto, R.Z. Valiev, T.G. Langdon, Microhardness measurements and the hall-petch relationship in an Al-Mg alloy with submicrometer grain size, Acta Metar. 44 (1996) 4619-4629.

[34] G.Z. Quan, Characterization for dynamic recrystallization kinetics based on stress-strain curves, in: P. Wilson (Ed.), Recent developments in the study of recrystallization, InTech, Croatia, 2013, pp. 61–88.

[35] R.S. Mishra, Z.Y. Ma, Friction stir welding and processing, Mater. Sci. Eng. R 50 (2005) 1-78.

[36] T. Shibayanagi, A.P. Gerlich, K. Kashihara, T.H. North, Textures in single-crystal aluminum friction stir spot welds, Metall. Mater. Trans. A 40 (2009) 920-931.

[37] J. Chen, R. Ueji, H. Fujii, Double-sides friction-stir welding of magnesium alloy with concave-convex tools for texture control, Mater. Des. 76 (2015) 181-189.

[38] S.H.C. Park, Y.S. Sato, H. Kokawa, Basal plane texture and flow pattern in friction stir weld of a magnesium alloy, Metall. Mater. Trans. A 34 (2003) 987-994.

[39] R. Nandan, G.G. Roy, T.J. Lienert, T. Debroy, Three-dimensional heat and material flow during friction stir welding of mild steel, Acta Mater. 55 (2007) 883-895.

[40] F.C. Liu, T.W. Nelson, In-situ grain structure and texture evolution during friction stir welding of austenite stainless steel, Mater. Des. 115 (2017) 467-478.

[41] Y. Morisada, T. Imaizumi, H. Fujii, Clarification of material flow and defect formation during friction stir welding, Sci. Tech. Weld. Join. 20 (2015) 130-137.

[42] E.O. Hall, The deformation and ageing of mild steel: III discussion of results, Proc. Phys. Soc. 64 (1951) 747-753.

[43] N.J. Petch, The cleavage strength of polycrystals, J. Iron Steel Institute 174 (1953) 25-28.

[44] Q. Liu, A simple and rapid method for determining orientations and misorientations of crystalline specimens in TEM, Ultramicroscopy 60 (1995) 81-89.

[45] M. Sachtleber, Z. Zhao, D. Raabe, Experimental investigation of plastic grain interaction, Mater. Sci. Eng. A 336 (2002) 81-87.

[46] Y.B. Tan, X.M. Wang, M. Ma, J.X. Zhang, W.C. Liu, R.D. Fu, S. Xiang, A study on microstructure and mechanical properties of AA 3003 aluminum alloy joints by underwater friction stir welding, Mater. Charact. 127 (2017) 41-52.

[47] N. Afrin, D.L. Chen, X. Cao, M. Jahazi, Strain hardening behavior of a friction stir welded magnesium alloy, Scr. Mater. 57 (2007) 1004-1007.

[48] J.A. del Valle, F. Carreño, O.A. Ruano, Influence of texture and grain size on work hardening and ductility in magnesium-based alloys processed by ECAP and rolling, Acta Mater. 54 (2006) 4247-4259.

[49] F. Roters, D. Raabe, G. Gottstein, Work hardening in heterogeneous alloys-a microstructural approach based on three internal state variables, Acta Mater. 48 (2000) 4181-4189.

[50] H. Mecking, U.F. Kocks, Ch. Hartig, Taylor factors in materials with many deformation modes, Scr. Mater. 35 (1996) 465-471.

[51] C.H. Cáceres, P. Lukáč, Strain hardening behaviour and the Taylor factor of pure magnesium, Philos. Mag. 88 (2008) 977-989.

[52] E.W. Lee, P.N. Kalu, L. Brandao, O.S. Es-Said, J. Foyos, H. Garmestani, The effect of off-axis thermomechanical processing on the mechanical behavior of textured 2095 Al-Li alloy, Mater. Sci. Eng. A 265 (1999) 100-109.

[53] S.C. Wang, Z. Zhu, M.J. Starink, Estimation of dislocation densities in cold rolled Al-Mg-Cu-Mn alloys by combination of yield strength data, EBSD and strength models, J. Microsc. 217 (2005) 174-178.

[54] M. Nakai, M. Niinomi, Y. Ishida, H.H. Liu, H. Fujii, T. Ninomiya, Heat treatment to improve the fatigue strength of friction stir welded Ti-6Al-4V alloy butt joint, Mater. Trans. 58 (2017) 1223-1226.

Fig. 1. (a) Schematic illustration of butt FSW processing, FSW geometry, and preparation of cross-section specimen for microstructural analysis; (b) preparation of specimens for tensile tests from the weld joint.

Fig. 2. Surface appearance and optical macrograph of transverse cross section of the weld joint.

Fig. 3. (a) EBSD IPF and (b) corresponding (101) and (111) PFs of BM.

Fig. 4. (a) EBSD micrograph of the TMAZ adjacent to the RS; (b-d) magnifications of areas marked by rectangles b, c and d in (a), respectively; (e) misorientation angles versus distances along the arrows marked in (b).

Fig. 5. (a) Positions for EBSD observations within the SZ; (b-f) EBSD micrographs obtained from top, center, and bottom of SZ-center, and RS and AS of SZ, respectively.

Fig. 6. (a) Schematic illustration of SPN and SD for each examined location within the SZ; (b-f) original and final rotated (101) PFs of top, center, and bottom of SZ-center, and RS and AS of SZ, respectively; (d) ideal simple shear texture components of bcc metals [30, 31].

Fig. 7. (a) Hardness distribution along transverse center line on the cross section of joint; (b) tensile properties of BM local specimens and SZ local specimens; (c) fractured specimen image of joint tensile specimen.

Fig. 8. Material flow patterns within the SZ during FSW on (a) the top-plane, (b) the mid-plane and (c) the bottom-plane [39, 40].

Fig. 9. Material flow field within the SZ during FSW.

Fig. 10. Microstructural features of BM, TMAZ, and all examined locations within the SZ of the joint: (a) average grain boundary spacing in TD; (b) length fractions of LAB; (c) misorientation angle distributions of boundaries; (d) average Taylor factors.

Table. 1. Chemical composition of the Ti-15-3 alloy plate (mass%).

Element Alloy	Ti	V	Cr	Al	Sn	O	Fe	N	H
Ti-15-3	Bal.	15.47	3.21	3.10	2.95	0.095	0.160	0.0085	0.025